ADVANCED OPTICAL MATERIALS
www.advopticalmat.de

Optical Poling of Ferroelectric Liquids

*Stefano Marni, Raouf Barboza, Noel Clark, Tommaso Bellini, and Liana Lucchetti**

Ferroelectric nematic liquid crystals combine fluidity, spontaneous polarity, optical birefringence, and strong nonlinear response, unlocking a rich landscape of phenomena and control strategies yet to be fully explored. Here, all-optical manipulation of polar domains and topological textures in ferroelectric nematic cells assembled from lithium niobate plates is demonstrated. In these devices, the photovoltaic response of the solid substrate couples to the fluid's polar director, enabling light-driven reorganization of the ferroelectric alignment. Under focused illumination in parallel-rubbed cells, the emergence of submillimeter-scale spiral-shaped radial domains is observed, in excellent agreement with the underlying material properties. Furthermore, it is shown that both domain structures and wall configurations can be reversibly reconfigured by varying light exposure, thereby tuning the degree of domain fragmentation and wall unpinning. These results establish light-induced polarization patterning as a versatile tool for dynamic control of nematic ferroelectric order, with promising applications in the design of reconfigurable linear and nonlinear photonic devices.

1. Introduction

The recently discovered polar nematic phase[1] (N_F) represents the first ferroelectric fluid with a workable viscosity and its peculiar combination of fluidity and polarity has opened the gate to many new phenomena. In this phase, the molecular arrangement breaks the $\mathbf{n} \rightarrow -\mathbf{n}$ mirror symmetry of the director—a unit vector that specifies the average molecular orientation—characterizing the conventional non-polar nematic phase. This feature leads to many peculiar properties, among which those related to the polar coupling to electric fields.[2–8]

Unlike ferroelectric solids, with which they share the high value of the spontaneous polarization $\mathbf{P}$ and the tendency of minimizing the energy by breaking up into domains of different orientation of $\mathbf{P}$[1], N_F have a liquid-like viscosity and exhibit an easily deformable fluid polarization field. This combination of properties is expected to generate many possibilities of spatially distributed polarization topologies controlled by external stimuli.

A certain degree of control over the polar topology can be exerted by taking advantage of confinement and of coupling with the confining surfaces.[2,9–11] Soon after the discovery of the new phase, it became clear that the contact between a ferroelectric nematic liquid crystal and a surface with in-plane polarity generates a preferred in-plane orientation of the polarization field at that interface, which leads to the formation of bulk fluid monodomains of high polarization in a sort of surface-induced ferroelectric poling.[2] The polar topology of cells with planar alignment also depends on thickness.[9] Surface coupling combined with the dominance of electrostatic over elastic interactions, generates polar monodomains in very thin cells and stripes of alternating polarization in thicker samples.[9,11] The creation of periodic polarization structures by photoalignment has been reported in 2023 by Mertelj and co-workers[12] who exploited the flexoelectric coupling between polarization and splay director deformations, to generate controlled polarization patterns. Intriguing topology as chiral meron-like structures have also been observed in quasi 2D ferroelectric nematic domains driven by the competition between polar and elastic anisotropies.[13] In the absence of bulk and surface aligning axes, polar domains delimitated by conic domain walls are instead observed.[10]

In this work we show the first evidence of the optical control of polar topology in ferroelectric nematic cells. This is obtained by building thin parallel plate cells with two ferroelectric lithium niobate crystals as confining surfaces. The photovoltaic response of these substrates leads to the accumulation of electric charges on the illuminated portions of the surface, thus acting as a local electro-optical transducer. This construction and effect have already been investigated in the case of the conventional nematic phase,[14] and a light-induced modulation of the nematic director following the profile of the surface charge-generated field has been demonstrated.[15] These experiments, performed in homeotropic cells, obtained a rather small tilt of the liquid

S. Marni, R. Barboza, L. Lucchetti
Dipartimento SIMAU
Università Politecnica delle Marche
via Brecce Bianche, Ancona 60131, Italy
E-mail: l.lucchetti@univpm.it
S. Marni, T. Bellini
Medical Biotechnology and Translational Medicine Dept.
University of Milano
Segrate 20054, Italy
N. Clark
Department of Physics
Soft Materials Research Center
University of Colorado
Boulder, CO 80305, USA

The ORCID identification number(s) for the author(s) of this article can be found under https://doi.org/10.1002/adom.202501378

DOI: 10.1002/adom.202501378

crystal optic axis, yielding an effective birefringence of the order of 10^{-2}, with the fast axis radially oriented from the beam center. The modest birefringence is due to the weak dielectric coupling of the nematic director. The appearance of spontaneous polarization **P** makes the electric field coupling of ferroelectric nematics enormously different, both in symmetry and amplitude. We previously investigated the response of sessile ferroelectric nematic droplets resting on ferroelectric substrates, and observed a variety of effects, including electromechanical instabilities[3] and induced sliding,[16] confirming the strong polar coupling with substrate surface charging. Here we exploit this coupling in thin cell geometry to generate modulation in birefringence and polarity that are unachievable with conventional nematics. Our results indicate optical manipulation as a route for the control of the fluid polar axes, a capability of interest in view of the realization of linear and non-linear photonic structures.

2. Experimental Section

The ferroelectric nematic liquid crystal used in this work is 4-[(4-nitrophenoxy)carbonyl]phenyl2,4-dimethoxybenzoate (RM734). It was synthesized as described in ref. [1] and its structure and phase diagram have already been reported.[1,3] In this compound the N_F appears through a weak first order phase transition upon cooling from the conventional higher temperature nematic (N) phase and exists in the range 133–80 °C.[1,3] The spontaneous polarization **P** of RM734 is either parallel or antiparallel to the molecular director **n**, defining the average orientation of the molecular axis, and exceeds 6 μC cm^{-2} at the lowest temperature in the N_F phase.[1]

As ferroelectric solid substrates we used 1 mm thick z-cut iron doped (0.1% mol) lithium niobate (LN) crystals (Pi-Kem). In these kinds of crystals, the polar axis is along the thickness of the slab. When they are exposed to light with a wavelength in the iron absorption spectrum, the surface charge significantly increases thanks to the photovoltaic effect,[17] which consists in the appearance of a photo-induced current according to the scheme $Fe^{2+} + h\nu \rightarrow Fe^{3+} + e^-$. The subsequent charge distribution that takes place inside the crystal gives rise to an internal electric field known as photovoltaic field. In the case of LN crystals as those used here, a saturated photovoltaic field $E_{PV} = (10.1 \pm 0.8)$ V μm^{-1} has been estimated based on photocurrent measurements.[14] Considering the dielectric permittivity of LN (85.2 along the polar axis), we can thus expect an induced saturation surface charge density of about 0.8 μC cm^{-2}.

LN crystals were used as bare substrates with no coating applied and were gently mechanically rubbed unidirectionally with optical paper. Cells were assembled with the two substrates rubbed in parallel or antiparallel directions and arranged so to have antiparallel polar axis, thus developing charges of the same sign at both the interfaces with the liquid crystal. This configuration will be referred to as *np/pn*, where *n* and *p* stay for negative and positive. Cells were then filled by capillarity with RM734 in the nematic phase at $T = 180$ °C keeping the liquid crystal flow in the direction of rubbing. The thickness d fixed either by 2.0 μm spherical spacers or by 3 μm thick mylar stripes, ranged from 1 to 6 μm as measured with interferometric techniques. Cells with thickness smaller than the spacers diameter result from small curvature of the substrates in the central part of the samples. The samples obtained were then put inside a temperature controller suitable for the polarizing optical microscope stage and cooled down to 120 °C with a cooling rate of 1 °C min^{-1}. In the rest of the manuscript cells with thickness $d \leq 2$ μm will be indicated as "thin," while all the others will be called "thicker."

A gaussian beam from a frequency doubled Nd:YAG laser ($\lambda =$ 532 nm) focused to a waist $w = 12$ μm with intensity in the range I = (50–450) W cm^{-2}, has been used to illuminate specific regions of the obtained cells by impinging on the bottom LN substrate at normal incidence (**Figure 1**a-ii,b-ii). Due to the absorption of iron-doped LN crystals in the green part of the spectrum, the intensity reaching the top substrate is 25% of these values.

The effect of light irradiation on the cell topology was investigated in real time by polarized optical microscope (POM) observations. Videos were recorded with a CCD camera mounted on the optical microscope, at a rate of 25 frames per second.

3. Results

Light irradiation affects all the tested cells when they are in the N_F phase, while no effect is observed in the N phase. Moreover, experiments similar to those described below performed on N_F cells built with two glass substrates, do not give any result thus excluding the direct action of the optical field on the liquid crystal. Both these observations indicate that the effect of light on the cells polar topology is the result of a coupling between the ferroelectric liquid and the ferroelectric LN substrates. Such coupling is mediated by the electric field existing in the cell due to the LN surface charging induced by light irradiation.[16]

3.1. Optically Induced Electric Field Between the Lithium Niobate Substrates

In our experimental conditions, the irradiated area is much smaller than the thickness of the LN crystals used as cell substrates (12 μm vs 10^3 μm), thus the two charged surfaces in each crystal can be approximately considered to form an electric dipole. The resulting electric field outside the directly irradiated crystal combines with the one generated by the second substrate in the region filled with the ferroelectric fluid. Due to light absorption in the first LN substrate, which exhibits an absorption coefficient $\alpha \cong 28$ cm^{-1}, the light that reaches the second substrate is 75% less intense. This is expected to reduce the surface charging by the same amount. The resulting situation is that of two positively charged circular areas with different absolute values and the shape of the electric field, in the absence of the ferroelectric fluid, is reported in Figure 1 for two different cell gaps: $d = 1$ μm (a) and $d = 5$ μm (b) (see Note S1 of the Supporting Information for details on the simulation).

In both cases, the field is along the vertical z axis in the center of the light spot, which is indicated as $r = 0$ (panels a-i and b-i). The vertical component E_z is approximately constant within the beam waist (marked by a green dashed line) and rapidly decays to zero at a longer distance from the spot center. E_z is uniform along the cell thickness for $d = 1$ μm (panel a-i) while it decreases moving from the bottom to the top cell surface for $d = 5$ μm (panel b-i) and the same holds for the in-plane component E_r (panels a-iii

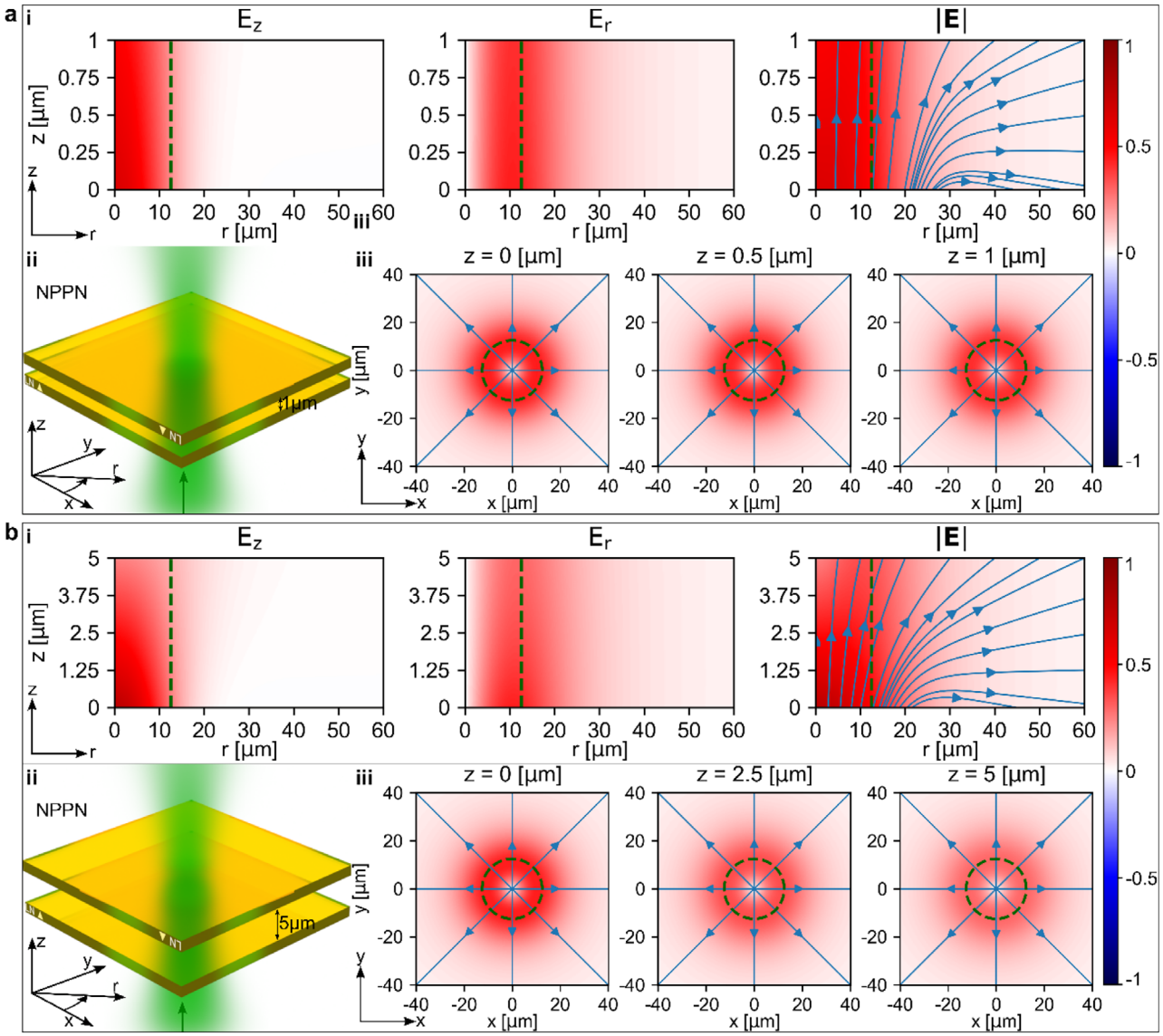

Figure 1. Electric field generated by light irradiation in the cell gap in the absence of the ferroelectric fluid and sketch of the cell illumination arrangement, a) for $d = 1$ μm and b) $d = 5$ μm. a-i,b-i) Vertical (E_z) and in-plane (E_r) components and field modulus along the vertical z-axis. Green dashed line marks the beam waist. Blue arrows represent the field lines. Note that the charge density imbalance due to light absorption generates a vertical component approximately uniform along the whole cell thickness. Panels a-ii and b-ii) Sketch of the cell before liquid crystal insertion and of the illumination arrangement. White arrows on the LN crystals sides indicate the LN polar axis. a-iii,b-iii) xy projection of **E** at different positions along the cell: bottom surface ($z = 0$), middle of the cell ($z = d/2$), top surface ($z = d$). Blue arrows represent the field lines, green circle marks the beam waist. Details of the simulation in the Supporting Information.

and b-iii). This latter is zero at $r = 0$, exhibits a first increase with the distance from the light spot center and then decays to zero on much longer distances with respect to E_z. The in-plane component of the electric field induced by light irradiation thus exhibits a radial profile in the whole irradiated area but in the very center where it vanishes, and such a profile extends over distances of several waists (panels a-iii and b-iii). Note that the two axes in the figure have different scaling, therefore the graphs representing the field lines do not preserve angles.

The specific effect of light irradiation depends on the original cell topology, which in turn is mainly affected by the thickness and by the mutual direction of rubbing on the two confining surfaces, as also reported in refs [9,18] for N_F cells realized with confining glass substrates. In the following we will describe the results obtained in different cells, separately.

3.2. Thin Cells with Parallel Rubbing

The unperturbed appearance of cells with thickness ranging between 1 and 2 μm and substrates with parallel rubbing is an approximately uniform monodomain texture with **P** in the direction of rubbing (**Figure** 2a). In these kinds of cells light irradiation gives rise to radial topological defects as those reported in

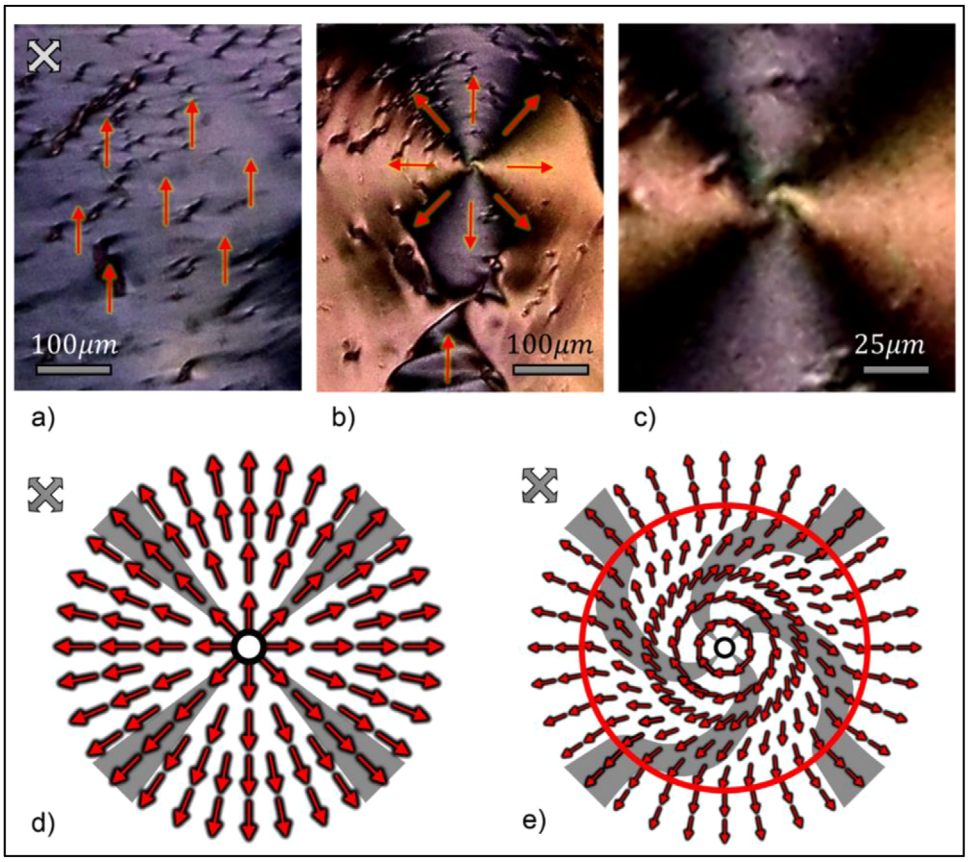

Figure 2. Effect of a focused light beam in a 1 μm thick planar cell with parallel rubbing. $T = 120$ °C. a) Cell texture before light irradiation. Red arrows indicate the polarization vector **P**, white crossed arrows represent the crossed POM polarizers. b) Maltese cross formed upon a few seconds light irradiation with $I = 100$ W cm^{-2}. The radial distribution of **P** is shown by red arrows. On the bottom of the panel, a polar domain with polarization opposite to that of the bottom arm of the cross, is visible. An additional defect with -1 charge is present at the intersection between these two domains (see Supporting Information). c) Zoom of the Maltese cross center, highlighting the spiralizing texture; d) sketch of the **P** profile in the case of neat radial alignment of N_F; e) sketch of the experimentally observed **P** profile. The red circle marks the border between the swirling and the radial regions. Panels a-c are extracted from Video S1 (Supporting Information).

Figure 2b, in agreement with the shape of the simulated optically induced electric field reported in Figure 1a.

Upon light irradiation the radial defect appears as a Maltese cross under polarizing optical microscope, extending in an area which is much larger than the light spot (Figure 2b). The radial distribution of **P** in the arms of the Maltese cross can be easily visualized in areas close to circular air bubbles[1] (Note S2 of the Supporting Information). The formation time of the Maltese cross depends on light intensity and is of the order of 1 s with small fluctuations from cell to cell (red symbols in Figure S3 and Note S3 of the Supporting Information). An example of the evolution of radial topology during light irradiation is shown in Figure S4 (Supporting Information). The inspection of the rotation direction of the Maltese arms in case of clockwise or counterclockwise rotation of the POM analyzer, proves that the observed defects have +1 topological charge. Specifically, we observed the rotation of the Maltese cross branches upon clockwise and counterclockwise rotation of the microscope analyzer. The cross arms rotate in the same sense as the analyzer, thus confirming the positive sign of the topological charge.

3.3. Radial Vortex Defects

The observed defects have the appearance of radial vortices. In these structures, the radial alignment of the polarization vector does not extend up to the central part of the defect, where the arms of the cross are bent and swirl around the core (Figure 2b,c). This configuration reduces the charge density related to splay deformation. Indeed, the volume charge density ρ can be calculated as:

$$p(r) = -\mathrm{div}\dot{p}(r) = -\frac{P}{r}\frac{\partial}{\partial r}[r\cos(\theta(r))] \quad (1)$$

where $\theta(r)$ is the angle that the polarization vector locally forms with the radial direction. In case of radial alignment of **P**, Equation (1) gives $\rho(r) = -P/r$, meaning that the density of the volume charge accumulated by the system diverges to infinity if the radial alignment extends up to the defect core, as in Figure 2d. The bent structure in the neighborhood of the defect center thus appears as a strategy adopted by the N_F to avoid a diverging bulk polarization charge. The evaluation of the volume charge density in the

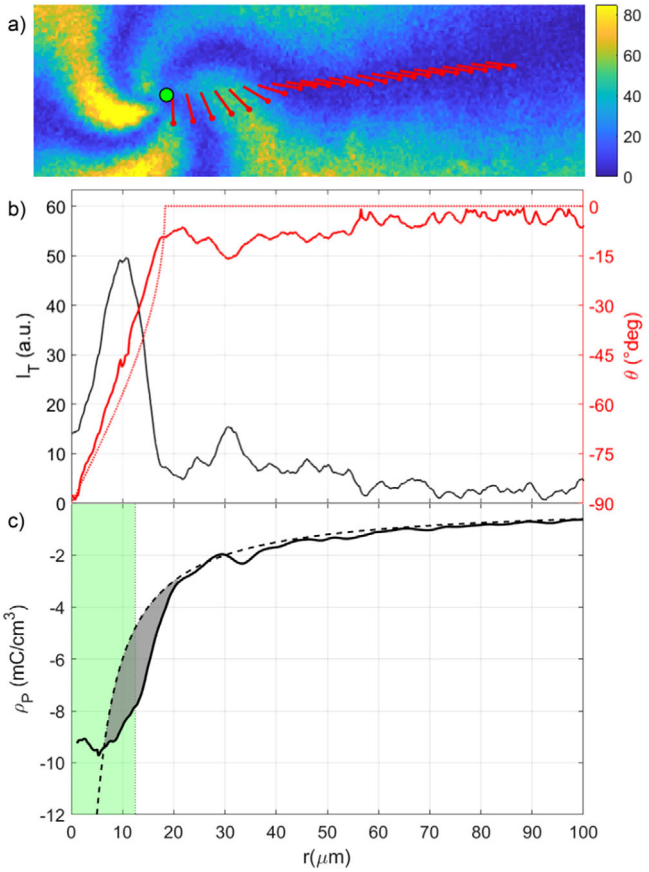

Figure 3. Estimation of the volume charge density accumulated in the radial defect. a) Branch of the Maltese cross selected for the analysis; the color code indicates the values of I_T obtained by averaging the Red and Blue channels of the image, the green dot is positioned at the intersection of the four arms and red arrows indicate the polarization vector **P** resulting from the analysis; b) transmitted intensity between crossed polarizers I_T along the selected branch versus distance from the cross center (black solid line) and angle $\theta(r)$ between **P** and the radial direction, calculated from I_T (solid red line). The dotted red line represents $\theta(r)$ as evaluated from Equation (5) (see text); c) volume charge density $\rho(r)$ versus distance from the cross center evaluated from experimental data (solid black line) and calculated in the case of radial alignment over the whole defect (dashed black line). The green area represents the beam waist. The gray color marks the region where the experimental charge density is larger than the one calculated for neat radial alignment of **P**.

configuration observed experimentally, is shown in **Figure 3**. It is based on the analysis of the POM image of the Maltese cross center from which the transmitted intensity I_T between crossed polarizers is extracted and used to quantify $\theta(r)$, as shown in Figure 3a for $T = 120$ °C and $I = 90$ W cm^{-2}. The angle between **P** and the radial direction is reported in Figure 3b (solid red line) together with I_T (solid black line), as a function of the distance from the defect center. $\theta(r)$ is 0 for $r \gtrsim 20$ µm and decreases to $-\pi/2$ as r approaches 0. An example of the resulting charge density $\rho(r)$ is plotted in Figure 3c (solid line) where it is compared with the curve $\rho(r) = -P/r$ (dashed line). The two curves overlap at a large distance from the core. Approaching the defect center, both the charge densities increase but the one corresponding to the experimentally observed configuration saturates to a finite value close to $r = 0$. Noteworthy, for $r \leq 20$ µm there is a region where the experimental charge density is larger than the one corresponding to total radial alignment (gray area in Figure 3c). This is a consequence of the saturation of $\rho(r)$ at $r = 0$ and of the constraint that the total charge carried by the N_F is conserved: a reduction in the $r = 0$ region with respect to dashed line (the neat radial structure) implies an increase somewhere else. Similar evaluations based on other Maltese crosses and/or made for different values of I gave similar results.

From the saturation value of $\rho(r)$ in Figure 3c combined with the cell thickness ($d = 1$ µm), it is possible to estimate the surface charge density, which is of the order of 1 µC cm^{-2}, i.e., comparable to the surface charging of the irradiated LN crystal ($\sigma_{LN} \approx 0.8$ µC cm^{-2}, see Experimental Section). This suggests that the charge accumulated by the N_F in the swirling area is intended to balance the charge on the LN surface. This cannot but occur via a tiny vertical tilt of the **P** axis depositing a **P**·**u** amount of charge on the LN surface (**u** is a unit vector normal to the N_F/LN interfaces). In the central region of the Maltese cross the optically induced electric field is thus zero, being compensated by another field opposing the radial alignment. Such an additional field is the depolarization field generated by the N_F itself. This is clearly indicated by the vortex structure of **P** sketched in Figure 2e, which cannot be a structure of the electric field. Since in the presence of an electric field the N_F polarization vector **P** aligns parallel to it, this behavior is compatible only with a vanishing total electric field in the swirling region.

Both the depolarization field $\mathbf{E}_{NF}$ and the field due to LN charging in the presence of the ferroelectric fluid, $\mathbf{E}_{LN}$, can be evaluated with the aid of the Gauss theorem considering a cylindrical surface as the one sketched in **Figure 4a**. Because of fluid superscreening,[4] the N_F cancels the field components perpendicular to the interfaces with LN, an insulating crystal, thus the electric field flux is different from zero only through the lateral cylindrical surface and the Gauss theorem reads: $E(r)2\pi rh = \frac{Q_{int}}{\varepsilon}$, being h the height of the cylindrical surface (equal to the thickness d of the cell), ε the product between ε_0 and the N_F relative dielectric permittivity and Q_{int} the total charge enclosed by the surface.

To understand how the interplay between the LN and N_F electric fields yields the observed vortex topology, it is convenient to introduce three distances from the center of the Maltese cross: R_W defined as the radius of the swirling area (where $\theta(r)$ is different from 0); R_{LN} defined as the extension of the LN charging (which is comparable, but not necessarily equal, to the beam waist), and R_M defined as the length of the smallest among the four branches of the cross, which represents a measure of the total extension of the radial vortex. Both R_W and R_M (Figure 4b,b') can easily be measured from POM images. Figure 4c reports their dependence on the laser intensity I extracted from images taken 20 s after the beginning of irradiation, at $T = 120$ °C. In these conditions the light induced topology exhibits its equilibrium texture and the LN surface charging can be considered saturated. While R_M increases linearly with I, R_W is constant within the experimental errors with an average value ($R_W = 18$ µm) slightly larger than the beam waist.

It is useful to compare the value of the field E_{LN} generated by LN upon light irradiation to that of the depolarization field E_{NF} corresponding to total radial alignment of **P** in the vortex defect (as in Figure 2d), in the different regions defined by R_W, R_{LN}, R_M.

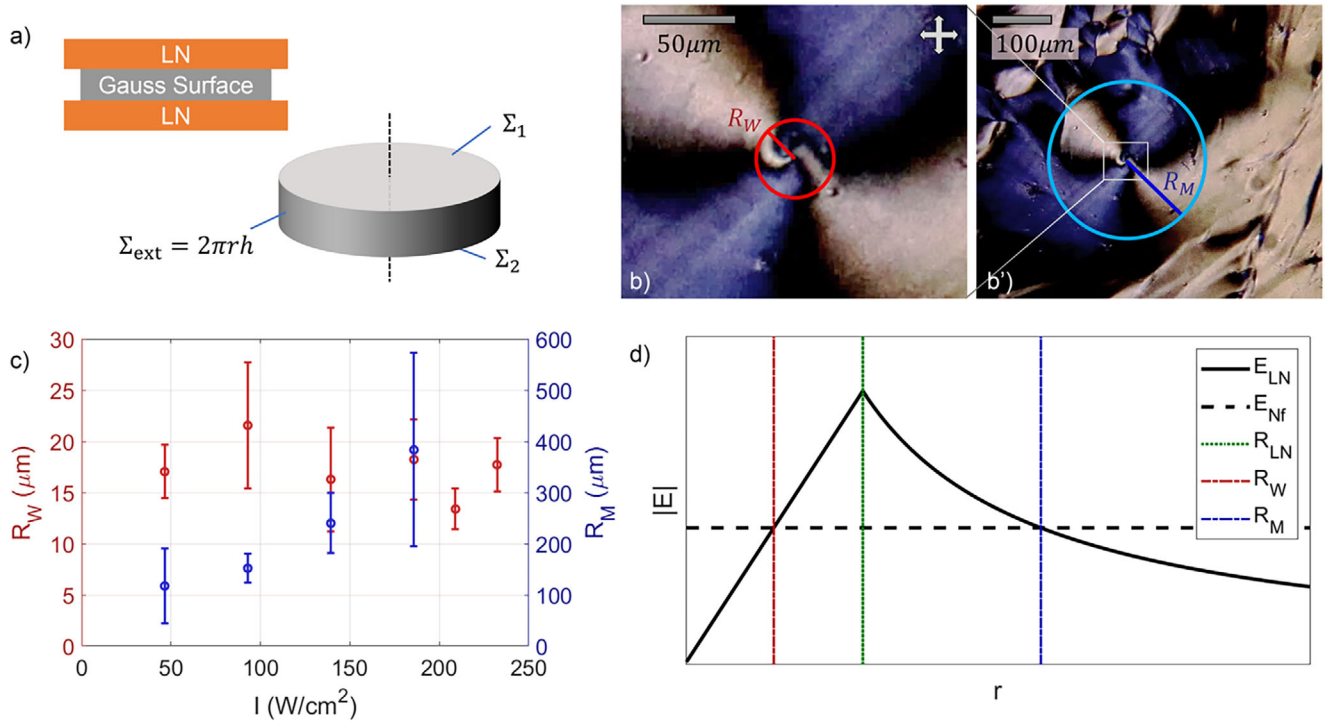

Figure 4. a) Cylindrical Gauss surface used for calculating the electric fields at play; b) radius of the central swirling area, R_W; b') total extension of the Maltese cross, defined as the length R_M of the shorter arm. R_M also represents the radius of the cross; c) R_W and R_M as a function of light intensity in a 1 μm thick cell at $T = 120$ °C; d) comparison between the absolute value of the electric field generated by LN (solid black line) and that of the depolarization field generated in N_F for the neat radial alignment of **P** represented in Figure 2d (dashed black line). Colored vertical lines mark R_W, R_{LN} and R_M, respectively (see text).

The total charge generated by LN for $r < R_{LN}$ is given by $\sigma_{LN}\pi r^2$, being σ_{LN} the LN surface charge density. The electric field is thus given by: $E_{LN}(r) = \frac{r\sigma_{LN}}{2\varepsilon h}$, so it increases linearly with the distance r from the center of the irradiated region.

At distances $r > R_{LN}$ the electric field adopts the following expression: $E_{LN}(r) = \frac{\sigma_{LN} R_{LN}^2}{2\varepsilon hr}$, and it decreases with the distance from the light spot center as $1/r$. Note that in these evaluations the LN surface charging has been assumed to have a step like profile, being equal to the saturation value for $r \leq R_{LN}$ and vanishing for $r > R_{LN}$.

To evaluate E_{NF} in the case of total radial alignment, we start from the total bound charge:

$$Q(r) = \int\int\int p(r)\,dV = \int_0^{r'} -\frac{P}{r'} 2\pi r' h dr' = -2\pi hPr \quad (2)$$

The depolarization field as evaluated through the Gauss theorem is thus constant over the whole defect area: $E_{NF} = -\frac{P}{\varepsilon}$.

A comparison between the absolute values of the two fields is shown in Figure 4d. The fields are equal for two specific values of r, which we identify as R_W and R_M. For $r < R_W$ the depolarization field generated by a radial alignment of **P** is larger than the field generated by LN, so this configuration is not sustainable by the system, which indeed assumes a different alignment. The same happens for $r > R_M$ where E_{LN} is too weak to induce the radial alignment of **P**. In the region between R_W and R_M, E_{NF} is instead smaller than E_{LN} and the polarization vector follows the radial alignment imposed by the photoinduced charging of the LN substrates.

This whole interpretation is coherent with the observed increase of R_W as light irradiation is terminated (Figure S4, Supporting Information). Indeed, as E_{LN} decreases, the first intersection point in the graph of Figure 4d shifts forward.

The evaluation of R_W and R_M based on these results, is in fair agreement with the experimentally observed trends reported in Figure 4c. Indeed, imposing $E_{LN}(R_W) = E_{NF}$ leads to:

$$R_W = \frac{2Ph}{\sigma_{LN}} \quad (3)$$

while $E_{LN}(R_M) = E_{NF}$ gives:

$$R_M = \frac{\sigma_{LN}}{2hP} R_{LN}^2 = \frac{Q_{LN}}{2\pi hP} \quad (4)$$

being Q_{LN} the total charge generated by light irradiation on the LN substrates surface. In conditions of saturated LN charging, σ_{LN} is independent on the light intensity I, and so is R_W. On the contrary, Q_{LN} depends on I since increasing the light intensity in conditions of saturation leads to the increase of the surface where the charge density reaches the saturation value. That is to say that R_{LN} increases with I, the specific dependence being of the form $R_{LN} \propto \sqrt{I}$.

From Equation (3) it is possible to estimate the saturation LN charge density. Using $h = (1.0 \pm 0.3)$ μm, $R_W = (18 \pm 4)$ μm and

$P(T = 120\ °C) = 5\ \mu C\ cm^{-2}$,[1] we obtain: $\sigma_{LN} = (0.6 \pm 0.3)\ \mu C\ cm^{-2}$ in fair agreement with the expected LN charging due to the photovoltaic effect.

From the compensation of the bound charge (Equation 2) and LN charge $Q_{LN}\ (r \leq R_W) = \sigma_{LN}\pi r^2$, it is instead possible to derive the angular profile of **P**:

$$\theta\,(r) = -\arccos\left(\frac{r\sigma_{LN}}{2hP}\right) \tag{5}$$

This is represented in Figure 3b as a red dotted line, which well approximates the experimental profile (solid red line).

The described radial vortex has been observed also in 1–2 µm thick cells realized by reverting one LN substrate so that the photoinduced charges at the two interfaces with the liquid crystal have opposite sign, a configuration indicated as *np/np* (Note S4 and Video S2, Supporting Information). An additional configuration that allows obtaining radial vortices is that of thin N_F cells realized with one LN crystal and an unrubbed glass slide as confining surfaces (Figure S7 and Note S4 of the Supporting Information). On the contrary, if the glass slide is treated to impart planar alignment to the RM734 molecules, light irradiation does not result in the formation of a Maltese cross with radial **P** distribution. Indeed, in this case the branches of the cross are replaced by twisted domains of opposite handedness, separated by a faceted wall (Figure S8 and Video S3 and Note 4 of the Supporting Information).

The radial vortex observed in this manuscript are most likely an all-optical polar version of the umbilical defects (or umbilics) obtained in liquid crystal light valves, i.e., homeotropic nematic liquid crystal cells with negative anisotropy, built with conductive substrates, one of which coated by a photoconductive layer.[17,19] Umbilics are selectively generated in these cells using a combination of electric and optical field. An external electric field lower than the Fredericks threshold for director reorientation is applied along the cell thickness and a Gaussian beam is shone on the photoconductive coated side of the cell. This produces a bell-shaped profile of the applied voltage, higher in the center of the illuminated area. By increasing the bias voltage or the beam intensity, the peak value of the effective voltage eventually overcomes the threshold. As a consequence, the liquid crystal molecules undergo a small tilt in a neighborhood of the irradiated area, giving rise to an umbilical defect. The polar umbilics we obtained here are due to a modulation of the polar optic axis, which is all-optical thanks to the natural radial distribution of the electric field induced by the LN photovoltaic charging. Due to the electrostatic constraint peculiar to ferroelectric nematic fluids, they correspond to complete rotation of the optical axis in the plane of the cells, thus resulting in patterns in which the whole available liquid crystal birefringence is modulated.

Our analysis shed light on the origin of the polar vortices realized very recently in N_F cells built with glass confining surfaces, by means of a photo-aligning technique followed by a thermal annealing treatment[18,20] The defect core exhibits the same spiral distribution reported in this manuscript and, though the topology of the defect is not analyzed, this is phenomenologically interpreted as a strategy to minimize charge accumulation. The work focuses instead on the ability of these defects to act as linear and nonlinear q-plates, which highlights the interest related to the realization of similar polar topological structures. The main advantage of the vortices generated in the present manuscript is that they do not require lengthy treatment of the cell substrates and are easily obtained in selected cell regions, in less than 1 s upon irradiation with a focused light beam. Moreover, contrary to those obtained by photoalignment, they can be quickly reconfigured by varying the beam position (Video S4, Supporting Information).

3.4. Thin Cells with Antiparallel Rubbing

In the case of antiparallel rubbing, 1–2 µm thick cells exhibit large domains separated by faceted walls (**Figure 5**a). These domains have a full π-twisted structure with opposite handedness, right-handed (RH) and left-handed (LH)[2,17] —with arbitrary specific attribution—as verified by decrossing the POM analyzer in opposite directions. Their behavior under the action of light is shown in Figure 5 and in Video S5a,b (Supporting Information), for $I = 130\ W\ cm^{-2}$ and $T = 120\ °C$.

When the light beam is shone on one of the two domains, say the RH one, a new subdomain forms in a few tenths of seconds. The features and domain walls are those of an LH domain (Figure 5b,c). Symmetrically, upon moving the light spot to the large LH π-twisted domain (Figure 5d), a RH subdomain appears. This new small domain progressively connects to the lower large, twisted domain with the same handedness, while the LH small domain formed previously decreases in size (Figure 5e,f). Both the subdomains created by light become smaller as irradiation stops and then remain stable for several hours.

Because of the polar nature of N_F, the π twisted domains connect the two cell surfaces by passing through a polarization perpendicular to the rubbing direction **R**, which is opposite in the case of RH and LH twists. Thus, these structures will be stabilized or destabilized by electric fields pointing perpendicular to **R**, depending on the twist handedness. We understand the observed change of handedness as a destabilizing effect that $\mathbf{E}_{LN}$, which is radial, exerts on portions of the N_F cell, namely those in which the electric field is opposite to **P** on the mid plane of the twisted structure. Because of the radial symmetry, this occurs only on one side of the beam, while in the opposite region the electric field is stabilizing. The subdomains in Figure 5b,c,d,e,f are indeed generated at opposite sides of the light beam (above in b,c and below in d,e,f).

A similar effect of change of handedness has been reported by Chen et al.[2] in the case of a static electric field orthogonal to the rubbing direction. There, the field preferred state with **P** largely directed along **E** appears in several places of the cell via heterogeneous nucleation, while the surfaces stay in their polar preferred minima.[2] In our case, the effect is similar despite the field is radial, which is most probably due to the easier rotation of **P** far from the boundaries, with respect to what happens on the surfaces where **P** maintains the original preferred orientation.

An inspection of Video S5b (Supporting Information) shows that moving the beam when this is positioned close to the faceted border of a polar domain results in a real-time dragging of the domain wall suggesting that the system uses the energy provided by light irradiation to expand the area of the states with lower energy. Such states correspond to regions where **P** is parallel to the optically induced electric field in the middle of the cell.

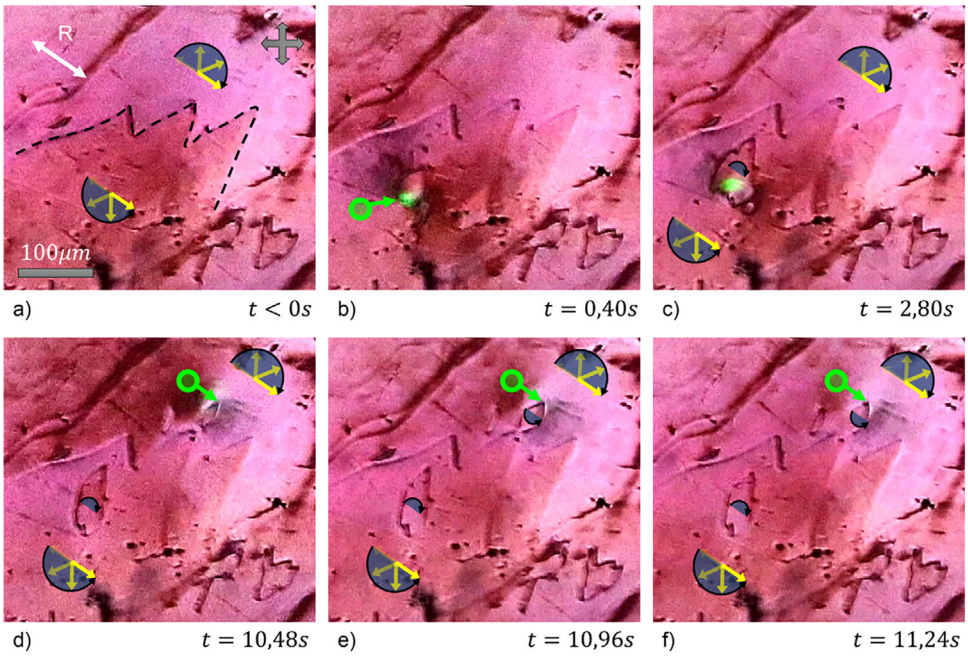

Figure 5. Effect of a static focused light beam in a 1 μm thick planar cell with antiparallel rubbing. a) Cell texture before light irradiation. White arrow indicates the rubbing direction, gray crossed arrows represent the crossed POM polarizers and yellow arrows represent the polarization vector **P** twisting along the cell thickness in opposite directions in the two domains. The faceted wall separating the two twisted domains is highlighted by a black dashed line. b) Light irradiation of a specific area in the RH region results in the formation of a small polar domain with faceted domain walls. c) The domain, which is π-twisted with opposite handedness with respect to the background, increases in size as light irradiation proceeds; d) moving the light beam in correspondence of the large LH region, a second small polar domain forms; e,f) as the illumination proceeds the domain connects to the large RH region in the bottom half of the image, meaning that it is twisted with the same handedness. Green arrow and circle highlight the light spot. (extracted from Video S5a, Supporting Information, $I = 130$ W cm^{-2} and $T = 120$ °C).

As the beam stops moving, the formation of new twisted domains is observed, as shown in Figure 5 and in Video S5a (Supporting Information).

3.5. Thicker Cells

Thicker cells ($d > 2$ μm) with parallel rubbing of the substrates, favor the formation of polar domains with **P** either parallel or antiparallel to the rubbing direction **R**. In some areas, these domains exhibit elongated shape, alternate positive and negative polarity in a way that each is surrounded only by the opposite type and are separated by domain walls that run approximately along **R** (**Figure** 6a). In other regions, large polar domains with **P** along **R** surround much smaller domains having opposite polarity (**Figure** 7a).

In these cells the coupling with the optically induced LN field is different than in thinner cells, and **P** does not follow $\mathbf{E}_{LN}$ along the whole thickness, as instead observed for thin cells with parallel rubbing. The profile of $\mathbf{E}_{LN}$ is here affected by the larger distance between the two LN substrates, as shown in Figure 1b, where the optically induced field is simulated for $d = 5$ μm. The main difference with respect to the case $d = 1$ μm, is that the field is not uniform along the cell thickness, being larger close to the directly irradiated substrate. This affects the liquid crystal response in a way that is shown in Figure 6 (for elongated polar domains of opposite **P**) and in Figure 7 (for large uniform areas surrounding small polar domains). Cell thickness in both figures is $d = 6$ μm.

In Figure 6b the light beam illuminates an elongated polar domain on the right-hand side of the image. This rapidly produces a reorientation of the liquid crystal director **n**, indicated by a change of the birefringence in the domain area above the light spot, where **P** is antiparallel to the local direction of $\mathbf{E}_{LN}$. As light irradiation proceeds, the variation of birefringence increases and extends to the adjacent domain, in the region where **P** and $\mathbf{E}_{LN}$ are locally antiparallel (green areas in Figure 6c). On longer time scales light illumination induces the formation of two small π-twisted domains where **P** is parallel to $\mathbf{E}_{LN}$ on the bottom substrate (gray arrows in Figure 6d). The width of these new domains increases in time and becomes stable after a few tens of seconds. The final stationary condition is shown in Figure 6d, where an imaginary green dashed line cuts the elongated polar domains in two regions: one reddish zone not perturbed by light irradiation, where **P** keeps its original direction locally parallel to $\mathbf{E}_{LN}$ and one greenish zone where **P**, initially antiparallel to $\mathbf{E}_{LN}$, rotated under the action of the field. Because of the radial symmetry of $\mathbf{E}_{LN}$, the two parts are alternated in the image.

The described behavior shows that illuminating the cell with a static beam for a certain time results in a less ordered texture. This suggests that the walls separating elongated polar domains are pinned to the surfaces and that the N_F polar coupling to the electric field does not overcome the pinning energy, as in the hard walls observed in reference.[17]

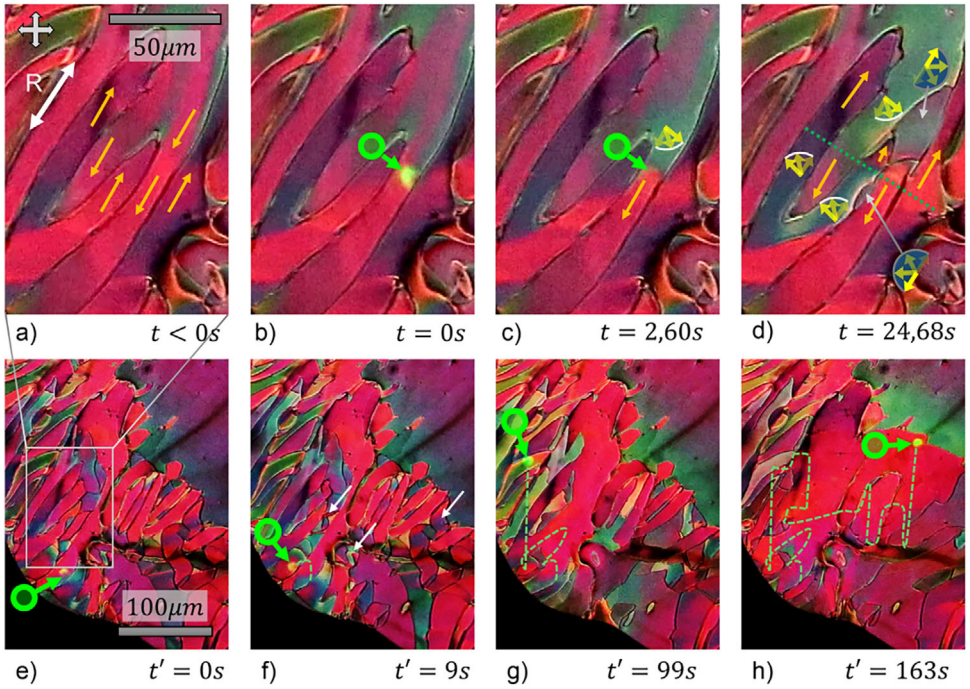

Figure 6. Effect of a focused light beam in a 6 μm thick planar cell with parallel rubbing. Region with striped domains of opposite polarity. a) Cell texture before light irradiation. Yellow arrows indicate the polarization vector **P**, gray crossed arrows represent the crossed POM polarizers; b) as light irradiation starts ($t = 0$ s) a change of birefringence in the domain area above the light spot, where **P** is antiparallel to the local direction of $\mathbf{E}_{LN}$, is observed; c) as irradiation proceeds the birefringence variation increases; d) final "stationary" condition as the beam is switched off: the green dashed line cuts the elongated polar domains in two regions: one reddish zone not perturbed by light irradiation and one greenish zone where **P**, initially antiparallel to $\mathbf{E}_{LN}$, rotated under the action of the field. Two new π-twisted domains, indicated by gray arrows, can also be observed; e) after 2 min, at $t' = 0$ s, light illumination starts again in the region highlighted by the green arrow; f–h) the light beam is randomly moved along the cell area (green dashed line), producing the disappearance of most of the elongated domains in favor of a more uniform texture. Green arrow and circle highlight the light spot. (extracted from Video S6a,b, Supporting Information, $I = 200$ W cm^{-2}, $T = 120$ °C).

However, the same walls can be displaced by continuously moving the beam over the cell area, as shown in Figure 6e–h, where a topological transition to a uniform polar texture can be observed. Indeed, the main part of the elongated domains is progressively substituted by a single uniform polar arrangement. This behavior suggests that dynamic illumination energizes and activates the system, which thus overcomes the pinning energy. Walls become free to move so to expand the domains with lower energy and the whole system rearranges its texture following the relaxation pathways opened by the energizing action of the moving beam. This can be appreciated by a close inspection of panels e–h, which reveals that polar domains where **P** is not uniformly aligned along **R** tend to disappear (panels f and g). Keeping on moving the beam produces a widening of the uniform area (panel h). The wall separating this uniform region from the twisted green-violet area on the right top of the figures shifts in response to the beam. The reddish color of the uniform large domain reveals that in this region **P** is along the rubbing direction **R** (parallel or antiparallel).

Occasionally, elongated domains positioned at a certain distance from the irradiated area exhibit a wavy texture (white arrows in Figure 6f). These structures are similar to those reported in ref. [19,21] and are described in Note S5 of the Supporting Information.

The effect of light irradiation in uniform areas of the same kinds of cells is reported in Figure 7. In Figure 7b, the light beam impinges on the cell close to the tip of a small lenticular domain having opposite polarization with respect to the uniform background. The domain areas where **P** is locally not aligned with $\mathbf{E}_{LN}$ begin to twist toward the field producing a color variation from red to green (Figure 7c–f). At the same time, distorted areas appear in the background, represented by green "wings" that born in correspondence of the light spot center (Figure 7c,d). These distortions increase in size and give rise to line defects at the interface with unperturbed areas (Figure 7e–h). As light irradiation proceeds, the small lenticular domain completely rearranges its polarization to match that of the background, thus losing its boundaries (Figure 7h). The light beam also affects the polarization in the tip of an elongated domain positioned at about 70 μm from the beam center, indicated by a white arrow in Figure 7h.

4. Conclusions

We reported the first evidence of the optical control of the polar topology in ferroelectric nematic liquid crystal cells with LN substrates. The number, shape and position of polar domains can be optically controlled, either with static or with dynamic illumination, with a focused beam of moderate intensity. In thin

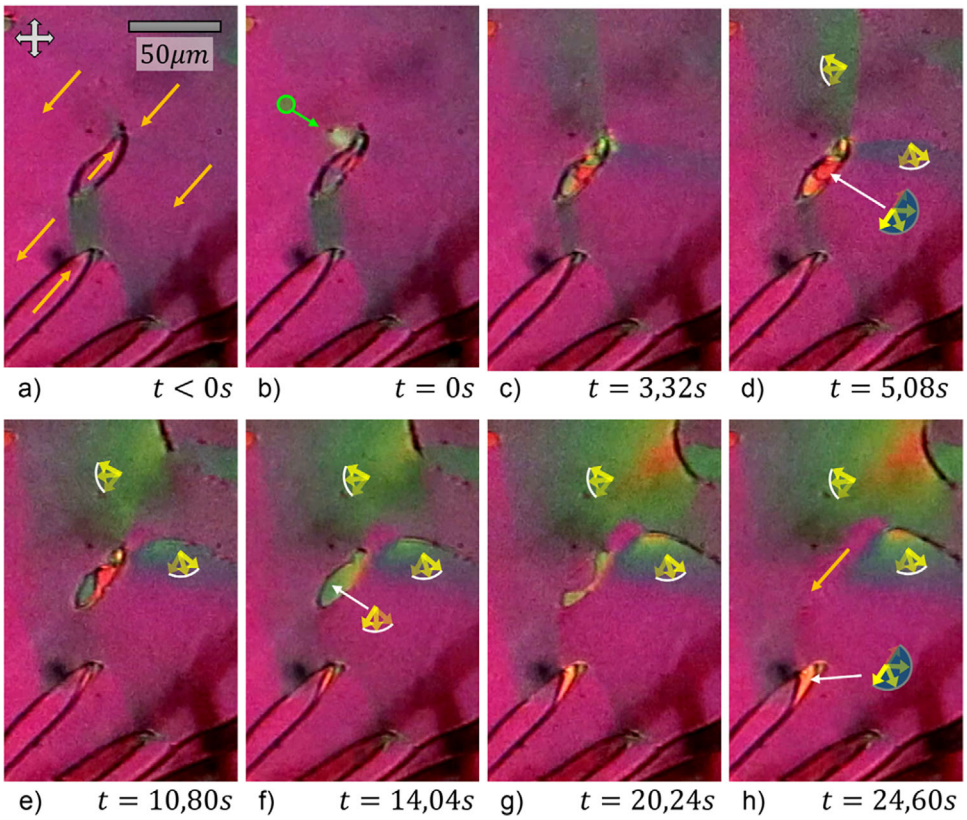

Figure 7. Effect of a focused light beam on a small, elongated domain in a 6 μm thick planar cell with parallel rubbing. The small domain lies on a large uniform area with opposite polarity. a) cell texture before light irradiation. Yellow arrows indicate polarization vector P, gray crossed arrows represent the crossed POM polarizers; b) at $t = 0$ s, light is switched on close to the small polar domain; c–f) domain areas where P is locally not aligned with E_{LN} begin to twist producing a color variation from red to green. Distorted areas also appear in the background, represented by green "wings" that born in correspondence of the light spot center; e–h) as irradiation proceeds, the green distorted regions increase in size and line defects form at the interfaces with unperturbed areas. In the meantime, the polarization of the small domain completely rotates to match that of the background (h). The white arrow in h) marks an elongated polar domain positioned about 70 μm from the light spot, which tip is affected by light irradiation. Green arrow and circle highlight the light spot. $I = 200$ W cm^{-2}, $T = 120$ °C.

parallel-rubbed cells, we observe the emergence of submillimeter-scale spiral-shaped radial domains, in excellent agreement with the underlying material properties, which we quantitively describe based on the minimization of the electrostatic charge density.

The action of light on the N_F liquid crystal is mediated by the electric field optically induced in the region between the LN plates. Such a field is confined in a neighborhood of the irradiated area, therefore, by varying the position of a focused beam we generate localized electric fields in specific locations of the N_F cell. This allows affecting the polar domain distribution—by creating and/or cancelling polar domains—in selected areas of the samples. The optically induced field can be quickly reconfigured in different positions, thus allowing a "real time" poling of the polar cells.

The localized electric field has a natural radial symmetry, which is not easy to obtain with external electrodes. This feature allows an unprecedented easy and fast realization of reconfigurable polar radial vortexes in specific regions of sufficiently thin cells. Indeed, light irradiation of 1–2 μm cells with parallel rubbing induces the formation of vortex-like defects with radial symmetry and spiral-shaped center, a polar version of umbilical defects found in conventional nematic liquid crystals under proper experimental conditions.[] Similar polar structures obtained by photoalignment and annealing in ferroelectric nematic liquid crystals, have been recently proved to act as linear and nonlinear q-plates.[18] In our experimental conditions the formation of several vortices in different locations of the same cell through multiple beam irradiation, is foreseen and is expected to allow the fast, single-step realization of reconfigurable, multiple polar q-plates. This would also give easy access to the study of how these topological structures interact with each other.

The demonstrated capability of light-induced polarization patterning opens a new route for controlling the ferroelectric polarization with potential toward the design of linear and nonlinear photonic structures. Overall, our study puts the basis for optical domain engineering in polar liquids and for the research of novel topological textures controlled by light.

Supporting Information

Supporting Information is available from the Wiley Online Library or from the author.

Acknowledgements

Part of this research was sponsored by the Army Research Laboratory and was accomplished under Grant Number W911NF-24-1-0252. The views and conclusions contained in this document are those of the authors and should not be interpreted as representing the official policies, either expressed or implied, of the Army Research Laboratory or the U.S. Government. The U.S. Government is authorized to reproduce and distribute reprints for Government purposes notwithstanding any copyright notation herein.

Conflict of Interest

The authors declare no conflict of interest.

Data Availability Statement

The data that support the findings of this study are available from the corresponding author upon reasonable request.

Keywords

ferroelectric nematic liquid crystals, lithium niobate, polar domains, radial vortex

Received: May 5, 2025
Revised: June 25, 2025
Published online: August 11, 2025

[1] X. Chen, E. Korblova, D. Dong, X. Wei, R. Shao, L. Radzihovsky, M. A. Glaser, J. E. Maclennan, D. Bedrov, D. M. Walba, N. A. Clark, *Proc. Natl. Acad. Sci. USA* **2020**, *117*, 14021.
[2] X. Chen, E. Korblova, M. A. Glaser, J. E. Maclennan, D. M. Walba, N. A. Clark, *Proc. Natl. Acad. Sci. USA* **2021**, *118*, 2104092118.
[3] R. Barboza, S. Marni, F. Ciciulla, F. A. Mir, G. Nava, F. Caimi, A. Zaltron, N. A. Clark, T. Bellini, L. Lucchetti, *Proc. Natl. Acad. Sci. USA* **2022**, *119*, 2207858119.
[4] F. Caimi, G. Nava, S. Fuschetto, L. Lucchetti, P. Paiè, R. Osellame, X. Chen, N. A. Clark, M. A. Glaser, T. Bellini, *Nat. Phys.* **2023**, *19*, 1658.
[5] M. Tibor Máthé, B. Farkas, L. Péter, Á. Buka, A. Jkli, P. Salamon, *Sci. Rep.* **2023**, *13*, 6981.
[6] Y.-T. Hsiao, I. Nys, K. Neyts, *Soft Matter* **2023**, *19*, 8617.
[7] Md S. H. Himel, K. Perera, A. Adaka, P. Guragain, R. J. Twieg, S. Sprunt, J. T. Gleeson, A. Jákli, *Adv. Funct. Mater.* **2025**, *35*, 2413674.
[8] M. Tibor Máthé, H. Nishikawa, F. Araoka, A. Jákli, P. Salamon, *Nat. Commun.* **2024**, *15*, 6928.
[9] B. Basnet, M. Rajabi, H. Wang, P. Kumari, K. Thapa, S. Paul, M. O. Lavrentovich, O. D. Lavrentovich, *Nat. Commun.* **2022**, *13*, 3932.
[10] P. Kumari, B. Basnet, H. Wang, O. D. Lavrentovich, *Nat. Commun.* **2023**, *14*, 748.
[11] S. Marni, F. Caimi, R. Barboza, N. Clark, T. Bellini, L. Lucchetti, *Soft Matter* **2024**, *20*, 4878.
[12] N. Sebastián, M. Lovšin, B. Berteloot, N. Osterman, A. Petelin, R. J. Mandle, S. Aya, M. Huang, I. Drevenšek-Olenik, K. Neyts, A. Mertelj, *Nat. Commun.* **2023**, *14*, 3029.
[13] J. Yang, Y. Zou, W. Tang, J. Li, M. Huang, S. Aya, *Nat. Commun.* **2022**, *13*, 7806.
[14] S. S. Bonfadini, F. Ciciulla, L. Criante, A. Zaltron, F. Simoni, V. Reshetnyak, L. Lucchetti, *Sci. Rep.* **2019**, *9*, 1062.
[15] S. L. Schafforz, G. Nordendorf, G. Nava, L. Lucchetti, A. Lorenz, *J. Mol. Liq* **2020**, *307*, 112963.
[16] S. Marni, G. Nava, R. Barboza, T. G. Bellini, L. Lucchetti, *Adv. Mater.* **2023**, *35*, 2212067.
[17] T. Volk, *Manfred Wöhlecke Lithium Niobate: Defects, Photorefraction and Ferroelectric Switching, Springer Series in Materials Science*, Springer Science & Business Media, Berlin **2008**, *115*.
[18] N. Sebastián, R. J. Mandle, A. Petelin, *Liq. Cryst.* **2021**, *48*, 2055.
[19] R. Barboza, U. Bortolozzo, M. G. Clerc, S. Residori, E. Vidal-Henriquez, *Adv. Opt. Photonics* **2015**, *7*, 635.
[20] J.-T. Pan, B.-H. Zhu, L.-L. Ma, W. Chen, G.-Y. Zhang, J. Tang, Y. Liu, Y. Wei, C. Zhang, Z.-H. Zhu, W.-G. Zhu, G. Li, Y.-Q. Lu, N. A. Clark, *Nat. Commun.* **2024**, *15*, 8732.
[21] S. Yi, Z. Hong, Z. Ma, C. Zhou, M. Jiang, X. Huang, M. Huang, S. Aya, R. Zhang, Q.-H. We, *Proc. Natl. Acad. Sci. USA* **2024**, *121*, 2413879121.